


Article

Mixed-Phase (2H and 1T) MoS₂ Catalyst for a Highly Efficient and Stable Si Photocathode

Jemee Joe ^{1,†}, Changdeuck Bae ^{1,*,†} , Eunsoo Kim ¹, Thi Anh Ho ¹, Heejun Yang ¹, Jong Hyeok Park ^{2,*} and Hyunjung Shin ^{1,*} 

¹ Department of Energy Science, Sungkyunkwan University, Suwon 440-746, Korea; konji3024@gmail.com (J.J.); lovelygoogle@naver.com (E.K.); lananhho88@gmail.com (T.A.H.); h.yang@skku.edu (H.Y.)

² Department of Chemical and Biomolecular Engineering, Yonsei University, Seoul 120-749, Korea

* Correspondence: changdeuck@skku.edu (C.B.); lutts@yonsei.ac.kr (J.H.P.); hshin@skku.edu (H.S.)

† These authors contributed equally to this work.

Received: 31 October 2018; Accepted: 16 November 2018; Published: 23 November 2018



Abstract: We describe the direct formation of mixed-phase (1T and 2H) MoS₂ layers on Si as a photocathode via atomic layer deposition (ALD) for application in the photoelectrochemical (PEC) reduction of water to hydrogen. Without typical series-metal interfaces between Si and MoS₂, our *p*-Si/SiO_x/MoS₂ photocathode showed efficient and stable operation in hydrogen evolution reactions (HERs). The resulting performance could be explained by spatially genuine device architectures in three dimensions (i.e., laterally homo and vertically heterojunction structures). The ALD-grown MoS₂ overlayer with the mixed-phase 1T and 2H homojunction passivates light absorber and surface states and functions as a monolithic structure for effective charge transport within MoS₂. It is also beneficial in the operation of *p-i-n* heterojunctions with inhomogeneous barrier heights due to the presence of mixed-phase cocatalysts. The effective barrier heights reached up to 0.8 eV with optimized MoS₂ thicknesses, leading to a 670 mV photovoltage enhancement without employing buried Si *p-n* junctions. The fast-transient behaviors via light illumination show that the mixed-phase layered chalcogenides can serve as efficient cocatalysts by depinning the Fermi levels at the interfaces. A long-term operation of ~70 h was also demonstrated in a 0.5 M H₂SO₄ solution.

Keywords: photoelectrochemical water splitting (PEC); molybdenum disulfide; atomic layer deposition (ALD); *p-i-n* heterojunction; pinch-off effect

1. Introduction

The photoelectrochemical (PEC) splitting of water into oxygen and hydrogen offers green fuel from solar energy. It requires a semiconductor to absorb photons of visible light and to generate excitons, fast charge separation within the depletion layer followed by efficient charge transfer to the electrolyte. Employing thin layers of cocatalysts onto semiconductor surfaces can alter the surface energetics by bending the degree of energy bands and/or charge transfer kinetics [1]. By choosing suitable catalytic systems, moreover, the semiconductor can be protected from the solution environment [2]. Silicon (Si) has been spotlighted as a promising earth-abundant light absorber due to its small band gap of 1.12 eV and its viability in the electronic device industry, especially in the field of solar cells. Since the available photovoltage obtainable from a single Si junction is about 0.5 V and not enough for water splitting, which requires 1.23 V of minimum thermodynamic potential, additional bias should be required during the PEC operation. In the unbiased PEC configurations, therefore, multiple Si-based solar cells and tandem structures with wide-gap semiconductors are needed to boost the water splitting reactions [3]. In this study, we focus on the properties of photocathode as half-cell in the three-electrode configuration. To adapt Si as

a photocathode, however, surface protection is required to obtain corrosion stability along with the poor surface kinetics of Si. Much progress has been made mostly by modifying the semiconductor surface with various cocatalysts. In general, metals with a high work function (ϕ_w) are candidates because the barrier heights are increased; thus, chemically inert noble metals are favorable. Platinum (Pt) and Pt-group metals are the best-reported catalysts due to their large ϕ_w . Choi et al. decorated Pt particles on a silicon surface with an Al_2O_3 protection layer, showing 12 h of stable operation with a $27 \text{ mA}\cdot\text{cm}^{-2}$ saturated current density (J_{ph}) [4]. Zhao et al. modified silicon's morphology into black silicon, followed by deeply burying Pt nanoparticles inside the wires, which showed a 0.434 V onset voltage with a $22.5 \text{ mA}\cdot\text{cm}^{-2}$ J_{ph} [5]. Feng et al. fabricated a photocathode with series-metal deposition of Ti and Ni thin films before a Pt catalyst on *p*-Si, which exhibited an onset potential of ~ 0.3 V with a J_{ph} of $30 \text{ mA}\cdot\text{cm}^{-2}$ and 12 h of operation in an alkaline solution [6].

However, noble metals are expensive and not viable for large-scale production. Among the various candidates, transition metal dichalcogenides (TMD) materials have attracted significant attention due to its unique physical, optical, and electrical properties [7,8]. The lack of dangling bond of the basal plane layer enables the photovoltage (V_{ph}) be governed by the solid-state junction rather than its surface [9], which gives interest to many researchers to exploit the material to adapt in the field of photoelectrochemistry. Molybdenum disulfide (MoS_2) is the most widely studied material since it is cheap, earth-abundant and exhibits exceptional stability even in a strong acid [10], which makes the materials to be considered as an efficient catalytic material for the hydrogen evolution reaction (HER) [11–13]. Abundant structural defects (or edge sites) and high crystallinity and phase could lead to a highly active electrocatalyst [14]. Various fabrication methods, including mechanical and chemical exfoliation, that expose more edge sites of unsaturated S atoms have been studied [15,16]. Oh et al. showed the improved crystallinity of MoS_2 layer grown by atomic layer deposition (ALD), followed by sulfurization at high temperatures leads to better PEC performance, which are 630 mV reduction in the overpotential over Si and 24 h of stable operation [17]. It is found that the phase is the most affecting factors determining the electrocatalytic activity [18] and the metallic 1T phase has shown much higher activity in HER compared to semiconducting 2H phase [19,20].

Moreover, in PEC where solid-state properties are concerned, the detailed device configurations of semiconductor-based photoelectrodes has progressed: (1) Utilizing a metal-insulator-semiconductor (MIS) Schottky junction structure with a cocatalyst has proven to enhance the overall performance by modulating the band bending at the semiconductor surface. Recent studies have shown that the photocatalyst layer on the semiconductor increases the band bending, affecting the resulting V_{ph} [21,22]. The photocatalysts deposited on the semiconductor protect the surface from photocorrosion during an electrochemical reaction and secure chemically active/reaction sites on the surface, improving the charge transfer kinetics between the semiconductor and the solution. (2) To obtain a large V_{ph} , a buried *p*-Si/*n*⁺-Si junction in a semiconductor has been employed. Kwon et al. grew MoS_2 layers on SiO_2 , followed by transferring them to a Si substrate to form a *p*-*n* heterojunction, which exhibited a $24.6 \text{ m}\cdot\text{Acm}^{-2}$ J_{ph} at 0 V vs. RHE with a 0.17 V onset potential [23]. Seo et al. produced an onset potential of 0.36 V for a silicon photocathode with surface functionalization combined with Pt [24]. Benck et al. fabricated a silicon buried *p*-*n* junction with MoS_2 as the cocatalyst and showed an onset voltage of 0.32 V [25]. The presence of interfacial oxides, such as native SiO_x , not only provides the passivation for semiconductor surface states but also alleviates Fermi level pinning effects [26]. Despite the synergetic roles of interfacial oxides in water splitting, the direct deposition of materials with a high ϕ_w on Si/ SiO_x causes stability issues for long-term operation. (3) Researchers have demonstrated that the introduction of series-metal thin films, such as metal silicides, between Si and cocatalysts improved the stability. A Stanford University group showed a stability of up to 100 h at 0 V vs. RHE by a thin Mo_xSi and Mo layers on a Si *n*⁺*p* junction. Fan et al. additionally introduced thin Al_2O_3 layers on a Si junction to improve the stability from photocorrosion [27]. Although an amorphous Si-based photocathode with a high V_{ph} of 0.8 V has been reported, this was attributed to the different band gap of 1.7 eV [28].

Recently, we developed an ALD chemistry that can directly produce as-grown crystalline MoS₂ thin films on various substrates at low temperatures (250–300 °C) using inexpensive precursors (i.e., MoCl₅ + H₂S). ALD techniques have shown an exceptional capability for studying the critical thickness required for optimal HER operation [29]. Here, we describe that mixed-phase (1T and 2H) MoS₂ layers can be formed on Si as photocathodes via ALD for the PEC reduction of water. Note that we did not employ the extra phase-transition procedure from semiconducting 2H to metallic 1T phase. Without utilizing conventional series-metal interfaces, our simple *p*-Si/SiO_x/MoS₂ photocathode showed an efficient and stable operation during HERs. The present devices have spatially genuine architectures in three dimensions (i.e., laterally homo and vertically heterojunction structures). The effective barrier heights reached 0.6 eV with optimized MoS₂ thicknesses, leading to a V_{ph} enhancement of 670 mV without employing buried Si *p*-*n* junctions. A long-term operation of ~70 h was also demonstrated. We suggest that in general, 1T-2H mixed-phase layered chalcogenides could serve as efficient cocatalysts by depinning Fermi levels at the interfaces, resulting in efficient electron transfer mechanisms.

2. Results and Discussion

The unique device configuration of our *p*-Si/SiO_x/MoS₂ photocathode contrasts typical MIS photocathodes reported by other researchers (Figure 1). The electron-hole pairs are generated in the depletion region, mainly inside *p*-Si, and then transferred through the tunnel oxide to the thin metal interfaces toward cocatalysts in the electrolyte. The monolithic homojunctions consist of mixed-phase 1T and 2H MoS₂ that develop during the growth of MoS₂ via ALD. Depending on the degree of distortion in the S-Mo-S atomic planes, 2H and 1T phases exhibit different structural and electronic properties. The 2H phase has semiconducting properties and is more stable compared to other phases (e.g., 3R and 1T), whereas the 1T phase is metallic and unstable. A key mechanism may be the inclusion of an excess chlorine moiety along the MoS₂ basal plane upon incomplete reactions at low temperatures as probed by elemental analysis, X-ray photoelectron spectroscopy, and X-ray diffraction patterns [30]. We also demonstrated that as a result of the presence of Cl, the 1T phase was stable upon thermal annealing at 400 °C. Since the 1T phase of MoS₂ is metallic, the resulting MoS₂ layers as cocatalysts on the Si photocathode exhibit distinctively monolithic homojunctions with changes in the Φ_B laterally along the interfaces, as illustrated in Figure 1b. Our *p*-Si/SiO_x/MoS₂ photocathode makes the electron transfer pathway effective compared to a conventional MIS electrode, eliminating additional processes that are required for complicated interface engineering. Note that additional phase-conversion (2H-to-1T) and film-transfer processes were not necessary, thanks to the direct growth of the mixed-phase films on to the observer.

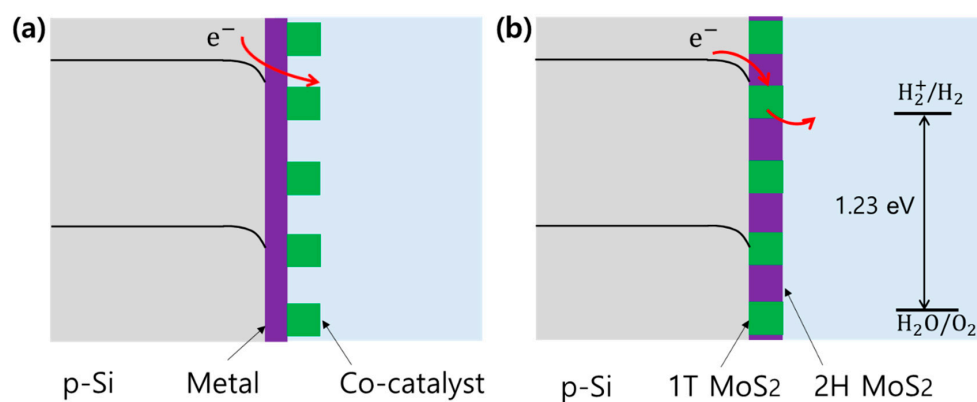


Figure 1. Device configurations of Si-based photocathodes: (a) Typical metal-insulator-semiconductor (MIS) Schottky junction photocathode with photocorrosion passivating and adhesion-promoting metal layers beneath the cocatalysts. (b) Our simple *p*-Si/SiO_x/mixed-phase (1T/2H) MoS₂ photocathode with laterally homo and vertically heterojunctions that includes an MIS junction inside.

The overall morphologies (Figure 2c–e) and the resulting thicknesses (Figure 2a,b,f,g,k) of MoS₂ on Si surfaces were reproducible as previously reported [29]. The layered-structural nature was shown by the Raman spectra (Figure 2j), and the mixed-phase (1T and 2H) structures were also observed via XPS spectra (Figure 2h,i). Initial cycles up to 100 ALD cycles resulted in several MoS₂ nanoflakes (diameter of ~10 nm). Most of the nuclei layers have parallel basal planes to the substrate surfaces, as shown in Figure 2a,f. The TEM of 300-cycled MoS₂ shows more vertically grown MoS₂ layers on the *p*-Si, as shown in Figure 2f. This growth mechanism was observed in thicker layers (1000 cycles in Figure 2g) and was identical to earlier work by some of the authors [29].

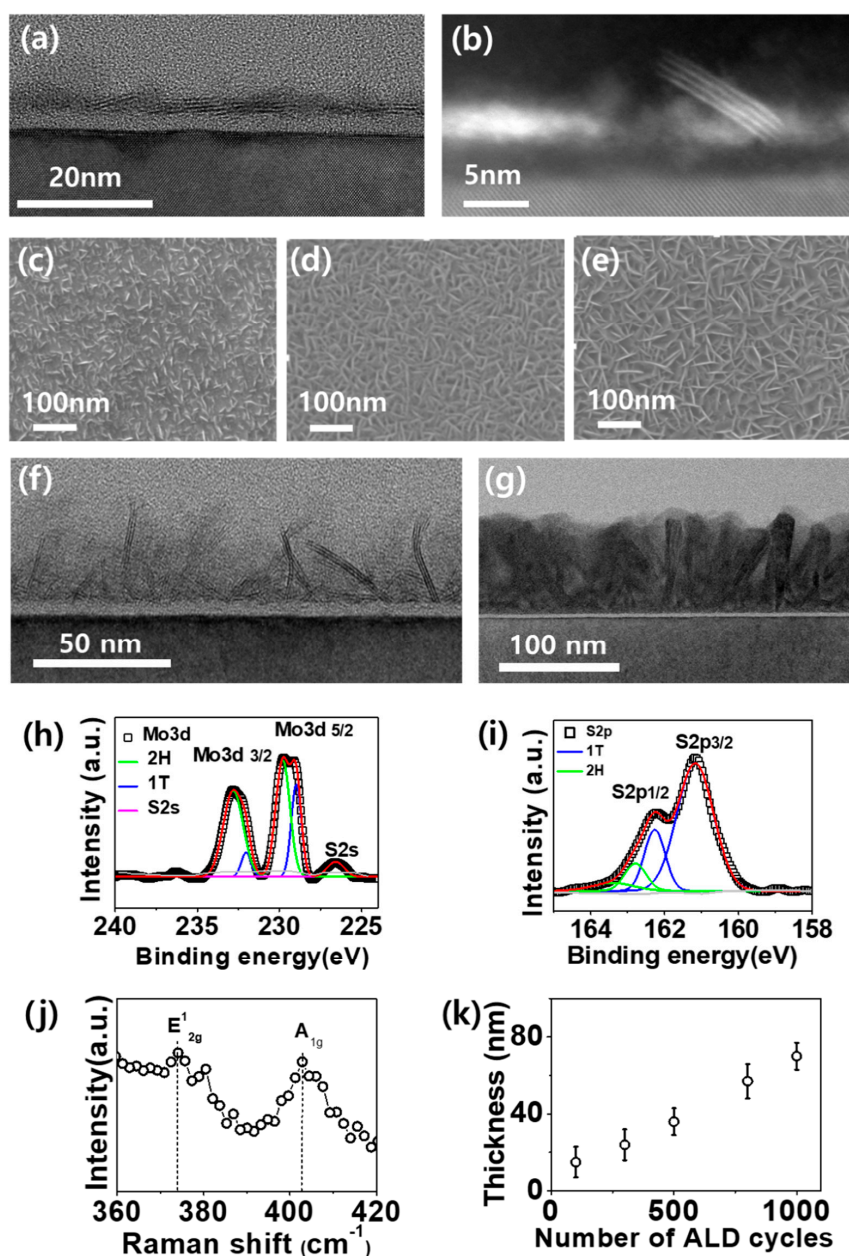


Figure 2. Preparation of *p*-Si/SiO_x/MoS₂ photocathodes via ALD as a function of deposition cycles. (a–g) Electron micrographs of MoS₂ of different thicknesses on Si: (a) Cross-sectional TEM and (b) STEM images of 100 ALD-cycled MoS₂ on Si; (c) SEM of 300 cycles; (d) SEM of 500 cycles; (e) SEM of 1000 cycles; (f) TEM of 300 cycles; (g) TEM of 1000 cycles showing a few layers of the MoS₂ stacked together. (h,i) High-resolution XPS spectra of Mo 3d and (k) S 2p core level peaks, and (j) Raman spectra of MoS₂ on Si. (k) Thickness as a function of ALD cycles, showing the linear growth rate.

We investigated the HER performance of our *p*-Si/SiO_x/MoS₂ photocathodes as a function of the MoS₂ thickness under illumination (100 mW·cm^{−2}), as shown in Figure 3. For a bare *p*-type silicon treated with HF, a photoelectrochemical reduction process begins at an onset potential of −0.12 V (which is defined when the photocurrent reaches 0.1 mA·cm^{−2}) with a J_{ph} of 24 ± 2 mA·cm^{−2}, which is consistent with other studies [31]. The corresponding measured V_{ph} is shown in Figure 3b, which is 0.11 ± 0.04 V and is much less than the theoretical maximum V_{ph} of Si of 0.48 to 0.5 V [32]. The gradual increase in J_{ph} near the turn-on potential (shown in Figure 3a (solid black line)) indicates the slow kinetics of the charge transfer processes. The decreased V_{ph} and the kinetics are attributed to the presence of surface states, followed by Fermi-level pinning (hereafter called FLP_{ss}) [33,34] at the surface/electrolyte interface and by the build-up of a surface oxide layer [23] and/or by electron traps by the complex surface chemistries that are associated with the formation of Si-OH bonds [35]. The photocathode produced via a few tens of ALD cycles of MoS₂ (data now shown) deposited on *p*-Si, which corresponds to less than 5 nm in thickness, showed negligible improvements in the PEC performance. This is partly due to the incomplete coverage of the silicon surface area since, from the initial ALD cycles, a number of seed layers of less than a few nanometer-thick nanoflakes randomly grow on Si. The photocathode produced with 100 ALD cycles, which is ~7 nm in average thickness, achieved an enhanced onset potential of 0.27 ± 0.02 V with an increased J_{ph} of 27.5 ± 0.5 mA·cm^{−2}. As shown in Figure 3b, the difference in the V_{ph} from the bare *p*-Si corresponds to the anodic onset voltage shift value of the 100-cycle ALD photocathode. The increase in V_{ph} is attributed to the surface states being reduced by the MoS₂ layers. The increase in a J_{ph} compared to bare *p*-Si is due to the reduced surface recombination, which is one of the limiting factors for photocurrents [36].

As the number of ALD cycle increased to 300, an onset potential shift to 0.24 ± 0.03 V was observed with an increase in the V_{ph} of 0.48 ± 0.01 V. As explained in our previous studies, after a certain number of flakes, additional MoS₂ layers grow in the vertical direction, covering the remaining exposed silicon surface to passivate from the electrolyte. Consequently, the Fermi level effect was almost alleviated, as V_{ph} reached the maximum value for *p*-Si. The maximum V_{ph} value of 0.80 to 0.67 V, which is much higher than the maximum V_{ph} limit (V_0) of *p*-Si and the J_{ph} of 30 mA·cm^{−2}, was attained at 500 ALD cycles (30 to 35 nm in average thickness). This is mainly attributed to the formation of a *p-i-n* heterojunction, including MIS between the *p*-Si/1T-MoS₂ partially within the bulk films, which will be discussed later in more detail.

The kinetic improvement that was partially due to an exposure of the edge sites is depicted in Figure 3c. The Tafel slope variations of 56 to 124 mV·decade^{−1} with the function of the number of ALD cycles were obtained by fitting the Tafel plots. Note that the Tafel slope of the 500-ALD-cycled photocathode, 90 mV·decade^{−1}, was larger than that of the 300-ALD-cycled photocathode, which is 56 mV·decade^{−1}; 56 mV·decade^{−1} for 300-ALD-cycle photocathode indicates the faster charge transfer rate. This value is in between the value of 2H-MoS₂ nanodots (61 mV·decade^{−1}) [37] and the value of 1T-MoS₂ (43 mV·decade^{−1}) [29] in terms of HER as electrocatalysts.

Our results revealed that the PEC performance with the 500-ALD-cycles photocathode does not necessarily exhibit the highest charge transfer kinetic property. Rather, surface energetics—i.e., a capability of electron/hole charge carrier's separation at near photoelectrodes' interface changed by the presence of a catalyst—can also contribute the PEC performances [38]. Increasing the number of ALD cycles from 600 to 800 degrades the PEC performance and the kinetics as shown in Figure 3a–c, which mostly came from the reduced light transmittance through the thicker MoS₂ layers. As mentioned in previous studies [39,40], the light intensity is necessary to obtain a surface V_{ph} , which turned out to be a function of the penetration depth. As the thickness increases to more than 40 nm, the penetration of light degradation induces a lower generation rate of electron-hole pairs. After 1000 ALD cycles, a 0.26 ± 0.01 V V_{ph} , which is similar or even less than for bare *p*-Si, was absorbed. An increased electrical and interfacial resistance degrades the PEC performance with the V_{on} voltage of −0.17 V was observed. The summary of important parameters for HER in PECs is shown in Table 1.

Note that our observation of the reduced PEC performance in thicker Cl-doped MoS₂ differs from recent works with MoS_xCl_y grown by chemical vapor deposition.

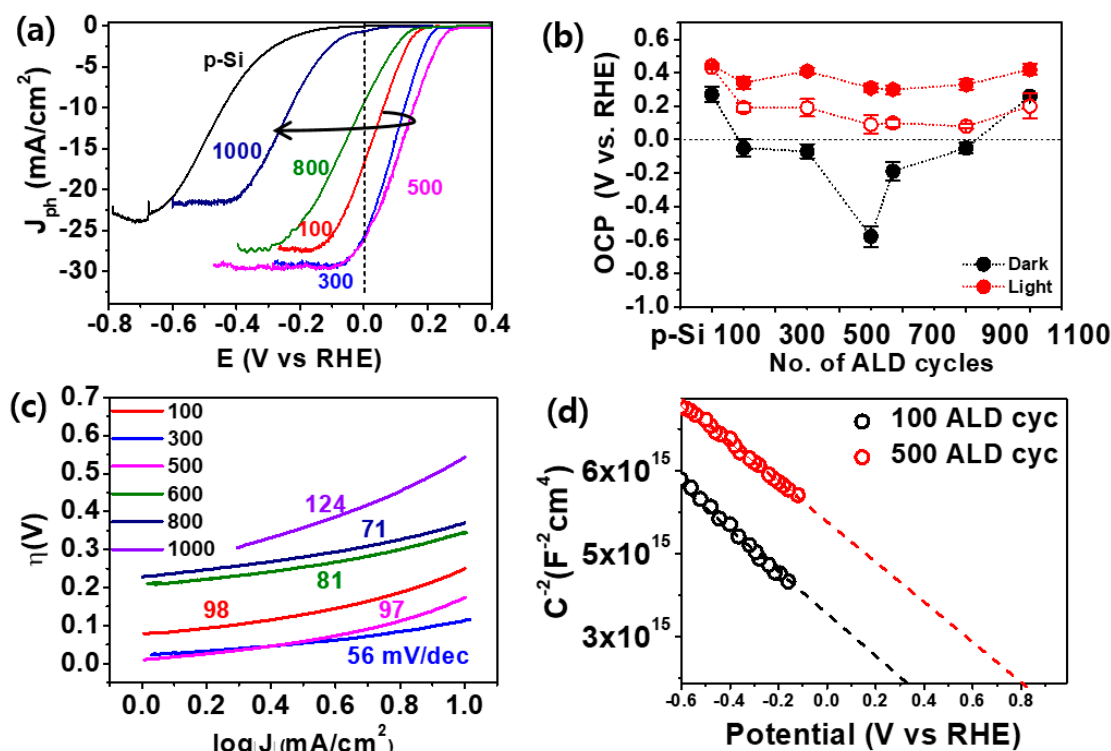


Figure 3. PEC performance of *p*-Si/SiO_x/MoS₂ photocathodes with different numbers of ALD Cycles. (a) Current density (J_{ph})—voltage (V) characteristic of the photocathodes under 1 sun illumination at a reverse bias. Anodic shifts of up to 0.35 V for the onset voltage (photocurrent onset of $0.1 \text{ mA} \cdot \text{cm}^{-2}$) were observed at approximately 500 cycles of ALD with a J_{ph} of $\sim 30 \text{ mA} \cdot \text{cm}^{-2}$. (b) Open circuit potential (OCP) measurement of our simple *p*-Si/SiO_x/MoS₂ photocathode for different MoS₂ thicknesses in the electrolyte. Each sample's OCP was recorded under dark and with 1 sun illumination. Red and black closed circles represent illumination and dark equilibrium, respectively. Red open circles are saturated voltages. The OCP shifted from positive to negative upon illumination, indicating the *p*-type property of the substrate. As the thickness increased, the flat-band potential increased from $0.11 \pm 0.02 \text{ V}$ (*p*-Si), and the maximum was obtained at 500 cycles for MoS₂, which was 0.8 to 0.67 V, as highlighted in the blue shadow. (c) Tafel curves of *p*-Si/SiO_x/MoS₂ of different number of ALD cycles. (d) Mott-Schottky plots of the *p*-Si/SiO_x/MoS₂ photocathode measured at reverse biases with a frequency of 200 kHz and a scan rate of $10 \text{ mV} \cdot \text{s}^{-1}$. The effective barrier heights of ~ 0.8 and 0.4 eV were estimated for 500 and 100 cycles, respectively.

Table 1. Summary of V_{ph} , V_{on} , J_{sc} , and J_{ph} of *J*-*V* characteristics, as shown in Figure 3.

	p-Si	100	300	500	600	800	1000
V_{ph}	0.11 ± 0.3	0.39 ± 0.04	0.48 ± 0.01	0.80 ± 0.02	0.49 ± 0.01	0.38 ± 0.01	0.26 ± 0.06
V_{on}	-0.12 ± 0.1	0.16 ± 0.02	0.24 ± 0.03	0.35 ± 0.03	0.27 ± 0.02	0.16 ± 0.01	-0.17 ± 0.02
J_{sc}	0.03 ± 0.05	17.18 ± 2.03	26.50 ± 1.40	26.70 ± 1.13	17.09 ± 1.63	10.03 ± 0.68	0.67 ± 0.26
J_{ph}	24.00 ± 1.31	27.00 ± 0.53	29.00 ± 0.62	30.00 ± 1.06	27.00 ± 2.30	26.00 ± 0.98	21.28 ± 1.08

To understand the junction characteristics further, we carried out the Mott-Schottky C-V analysis of our *p*-Si/SiO_x/MoS₂ photocathode (Figure 3d). Generally, C-V measurement can be a reliable method for the determination of built-in voltage (V_{bi}) and the doping density of *p*-*n* junction for Schottky junctions interface [41,42]. The C-V characteristics of 100- and 500-ALD-cycle photocathodes have been measured in the dark. Dotted lines are fitted to the experimental data. V_{bi} of the photocathodes can be estimated from the famous Mott-Schottky equation, where the intercepts of the straight lines yield 0.36

and 0.80 V at 200 kHz for 100- ALD cycle and 500- ALD-cycle photocathode, respectively. The slopes also indicate the photocathode of *p*-type conductivity. Kenny et al. pointed out the catalyst layer thickness dependence on the MIS junction characteristics utilizing partial screening charges and Debye length [43]. Another report by Fujii et al. stated that the thickness of the deposited semiconducting layer on another semiconductor of *p-n* heterojunction affects the depletion width, thus resulting in the V_{bi} variation [44]. The change in the build-up of the depletion region at the *p*-Si/MoS₂ (100- and 500-ALD cycles) interface junctions results in the increase of V_{bi} .

Indeed, our *p*-Si/SiO_x/MoS₂ photocathodes regulated the overall energy barriers and impedances of the total junctions. Accordingly, the stable operation under 1 sun illumination at a -0.3 V reverse bias and 0 V vs. RHE is shown in Figure 4a. The stable operation is due to the secure chemical contact formed between the *p*-Si/MoS₂ interface due to the ALD deposition method, which conformally deposited the layer on the silicon surfaces. Ding et al. experimentally confirmed the effect of a higher quality interface for 1T-MoS₂/Si by comparing the PEC characteristics of drop-casted 1T and CVD-grown 1T MoS₂ films, showing improved performance with a 0.235 V vs. RHE onset potential for the CVD-grown MoS₂ film on Si [45]. The metallic nanojunctions in our mixed-phase (1T and 2H) MoS₂ layers grown via ALD improved the stability for HER by reducing the contact resistance to Si. Upon stable operation of the *p*-Si/SiO_x/MoS₂ photocathode for 70 h under light, the resulting samples were analyzed by XRD, as shown in Figure 4b. Accordingly, the overall structures remained unchanged.

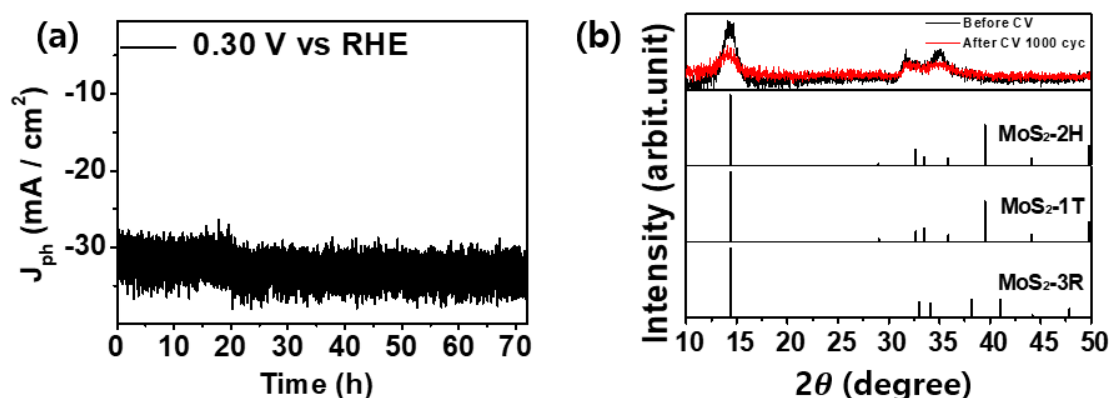


Figure 4. (a) Chronoamperometry of our *p*-Si/SiO_x/MoS₂ photocathode under illumination with an applied bias of -0.3 V vs. RHE and (b) XRD patterns of the photocathode before and after reaction.

While the overall electronic structure of the photocathode can be depicted as a *p-i-n* heterojunction, inside the MoS₂ film, the islands of embedded 1T phase nanostructures form a Schottky junction with *p*-Si. In Figure 5, the band alignments of *p*-Si/SiO_x/MoS₂ and the electrolyte in the nanoscale domain are drawn to explain an injected electron transport path that is energetically favorable, where V_o denotes the band bending at 0 bias, V_r is the applied reverse bias, ϕ_B is the Schottky barrier height, V_{ph} is the photovoltage, E_F is the Fermi level, and E_{Fn} is the quasi-Fermi level for electrons. For the band alignment at *p*-Si/MoS₂ interface, all the necessary parameters in terms of vacuum level and normal hydrogen electrode level in electrolyte of pH = 0.3 are shown in Figure S1, where the *p*-Si doping level is $\sim 1.6 \times 10^{15} \text{ cm}^{-3}$. The injected electron passes from 1T-MoS₂ to 2H-MoS₂, considering that 1T-MoS₂ exhibits a work function of approximately 4.2 eV, [46] which is not much different from that of the electron affinity of 2H MoS₂ (4.3 eV), and higher electrical conductivity compared with the 2H phase. Bai et al. studied the 1T/2H MoS₂ contact with different contact types and concluded that the edge-contact model exhibits a low tunneling barrier of 0.1 eV and even Ohmic contact in the case of having excess in-plane dangling bonds at the edge of 2H MoS₂ [47]. An important interpretation from the *J-V* characteristics of the PEC performance is that the conditions for bulk junction properties are fulfilled after 500 ALD cycles and the MoS₂ layer growth is already in the vertical direction. Therefore, in a situation of a high portion of 1T phase with an $\sim 10^{23} \text{ cm}^{-3}$ density of Cl ions, within the 2H

phase, there exists the 1T/2H MoS₂ phase as an edge-contact type, indicating that this electron transfer path model is valid.

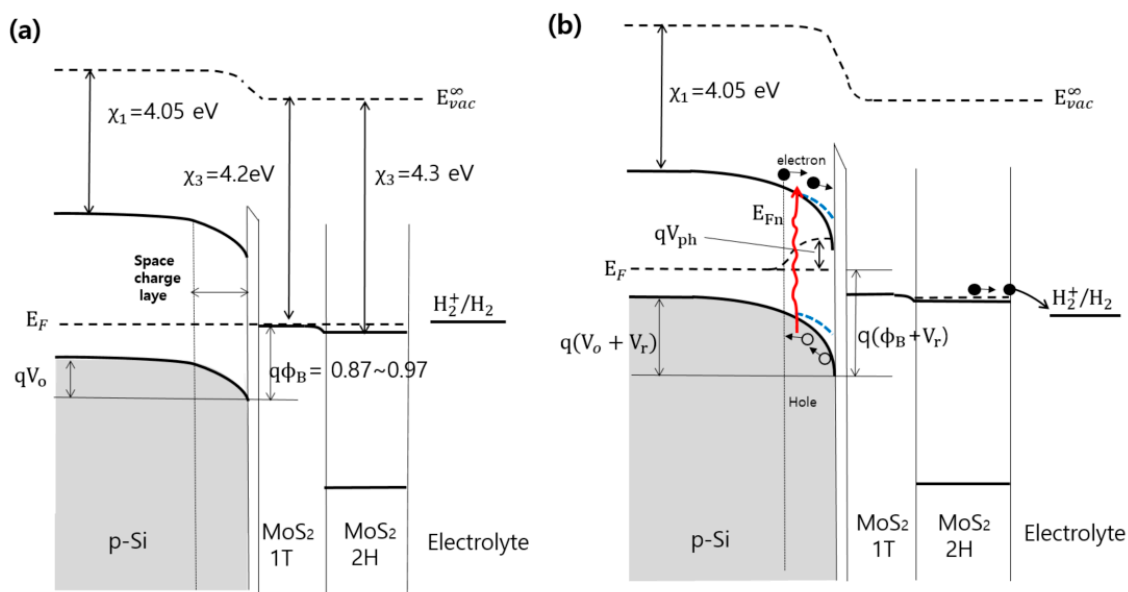


Figure 5. Energy band diagrams for energetically favorable exciton separation. (a) At thermal equilibrium and (b) under illumination at reverse bias.

Since the non-ideal growth characteristic of our ALD MoS₂ layers is well understood in the context of strong anisotropy in its covalency, the effects of active edge sites could be correlated in PEC operations. The initial number of layers forms in a nanoflake-like structure, mostly parallel to the substrate up to several tens of nm, followed by growing in the vertical direction. The layers progressively passivate the surface states of Si and decrease FLP_{ss}, which takes a significant portion for electron-hole pair recombination at the Si interfaces while maintaining the electrochemical activation sites for the HERs. The amount of surface recombination reduction leads to an increased V_{ph} [48], as observed in our experiments. The quantitative analysis of the surface energetics can be understood using Equation (1) [22],

$$\frac{n_s}{n_s^0} = \exp\left(-\frac{qV_0}{kT}\right) = \exp\left[-\frac{q(V_{app} + V_{ph} - V_{CB})}{kT}\right] \quad (1)$$

where n_s is the surface electron concentration at light, n_s^0 is the surface electron concentration at dark equilibrium, and γ is a constant at the interface, which is the ratio of energy states to the bulk, and V_0 is the amount of band bending at the junction interface. From Equation (1), we can deduce that the MoS₂ catalyst layer's thickness range is in the nanoscale domain, changes the surface charge concentration (here, electrons) of the Si, and modifies the surface energetics. The induced band bending also affects the photocurrent increment with the MoS₂ layer thickness to the certain point, which can be analyzed using the Butler–Volmer relation in Equation (2) [49].

$$i_n = i_0^n \left[\frac{n_s}{n_s^0} \exp\left(\frac{q\alpha_n\eta}{kT}\right) - \exp\left(-\frac{q(1-\alpha_n)\eta}{kT}\right) \right] \quad (2)$$

Here, i_n is the electron current, α_n is the electron charge transfer coefficient, and η is the overpotential. Based on the equation, the induced band bending modification explained above is an influencing factor for the exchange current and for the overpotential, η . The current induced within the bulk region is the sum of the current induced in the junction (depletion region) and the

current from the diffusion outside the depletion quasi-neutral region, which can be expressed by Equation (3) [50],

$$i_{ph} = qI_0 \left[\frac{1 - e^{-\alpha W}}{1 + \alpha L} \right] - qn_0 \frac{D_n}{L_n} \quad (3)$$

where i_{ph} is the photocurrent density, q is the electronic charge, I_0 is the monochromatic photon flux incident on the semiconductor, α is the light absorption coefficient of silicon, W is the depletion region, and L is the bulk diffusion length of Si. Since the depletion region variation was confirmed from the Mott-Schottky analysis in Figure 3d, we can conclude that for a certain MoS₂ thickness, the solid junction characteristics between the Si and the MoS₂ thin film play a role in enhancing the photocurrent. As a result, the spatially genuine 3D architectures (i.e., laterally homo and vertically heterojunction) with mixed-phases of 1T and 2H of MoS₂ mainly offer synergetic functions in PEC HERs.

The ALD deposited MoS₂ layers gradually alleviate the FLP_{ss} effect, and at the same time forming a bulk heterojunction interface. Considering the semiconductor p - n heterojunction utilized in PEC process, there are two types of V_{ph} values. One is at the p - n junction interfaces, and the second is on the surfaces, which are MoS₂/electrolyte interfaces [36]. It is confirmed in our previous study that our MoS₂ is insensitive to light (i.e., high doping concentrations). It is concluded then that the driving potential for the generated electron-hole pair separation and p - n junction interface-dominated V_{ph} . Now, considering the p - n heterojunction part in the p -Si/MoS₂, the built-in potential can be expressed by conventional solid-state physics in Equation (4) [51],

$$qV_{bi} = kT \ln \left[\frac{N_a N_d}{n_{in} n_{ip}} \right] + (\chi_p - \chi_N) + \frac{E_{GP} - E_{GN}}{2} - kT \ln \left[\frac{N_{VP} N_{CN}}{N_{CP} N_{VN}} \right] \quad (4)$$

where V_{bi} is the built-in potential, T is the temperature (294 K), q is the charge of an electron (1.6×10^{-19} C), k is Boltzmann's constant (1.38×10^{-23} JK⁻¹), N_a is the acceptor concentration of p -Si, N_d is the donor concentration of MoS₂, χ is the electron negativity for each type of semiconductor, E_G for the band gap, and N_{CN} and N_{VP} are the density of states of the conduction band and valence band, respectively. The values of MoS₂ except for the doping density were referred from the literatures [52–55]. The theoretical built-in voltage is 0.6 V. For the case of a Schottky barrier, it can be expressed as in Equation (5),

$$\phi_B = \frac{E_g}{q} + \chi - \phi_m \quad (5)$$

where ϕ_B is the Schottky barrier height, ϕ_m is the work function of 1T-MoS₂. The theoretical barrier height is therefore 0.87 to 0.97 V.

The open circuit potential (OCP) difference between dark and light directly indicates the V_{ph} observed, the amount of the band bending of the junction interfaces (Figure 6). Upon illumination, the amount of the Fermi level shift (V_m) is 0.8 V by observing a very sharp increase in the OCP as shown Figure 6a. This is distinctive in that typical PEC cells exhibit gradual increments when light turns on. The subsequent saturation is attributed to the recombination at the electrode/electrolyte interface, which results in 0.67 V (V_{ss}). Considering the physical dimension of metallic 1T MoS₂ of approximately 10 nm, which is much smaller than the depletion width, environmental Fermi level pinning (FLP_{ns}) is expected by nano-Schottky junctions of p -Si/1T MoS₂ although the surface states (FLP_{ss}) were passivated. Moreover, FLP_{ns} competes with both FLDP_{ox} and FLDP_{ox} followed by pinch-off, enabling effective tuning of the Schottky barrier, which results in the final value of the effective barrier height of 0.8 V (V_m). By observing a sharp increase in OCP, indeed, fast transient behavior occurred when light turns on, implying that FLP is negligible in the present electrochemical reactions. The OCP decay after turning off the light provided information on the generated electron-hole pair recombination at the

electrolyte interface and the carrier lifetime as shown in Figure 6b,c. The hole lifetime from the voltage decay is given by Equation (6) [56].

$$\tau_h = -\frac{kT}{q} \left(\frac{dV}{dt} \right)^{-1} \quad (6)$$

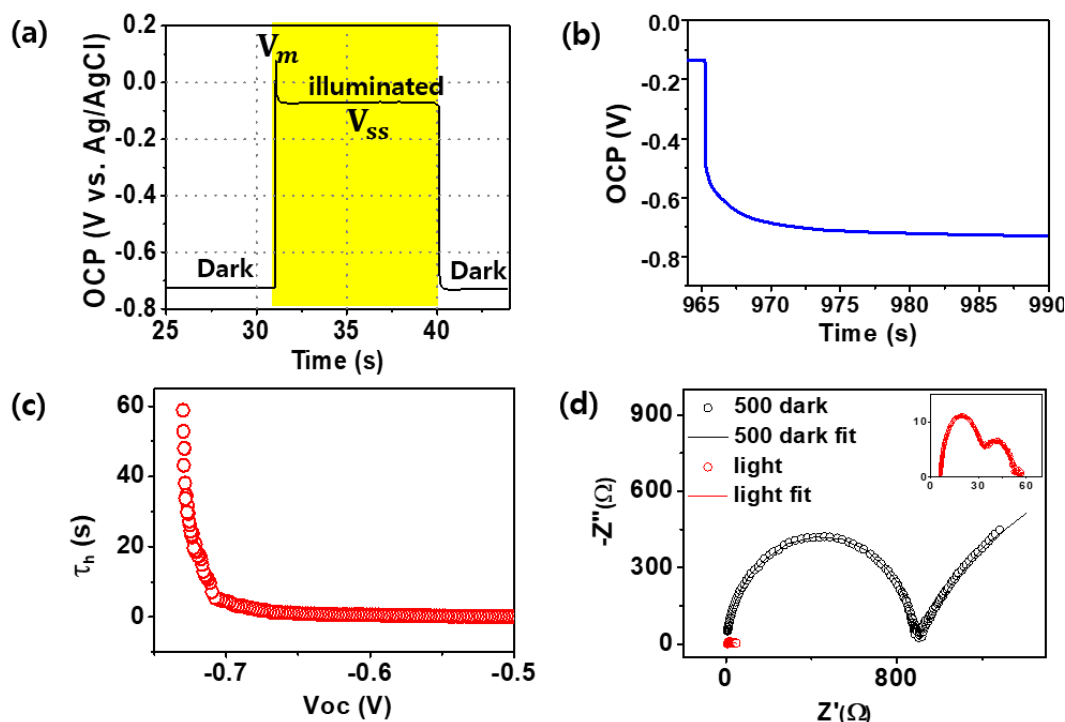


Figure 6. (a) OCP measurements of the 500 ALD-cycled MoS_2/Si photocathode. (b) OCP decay after illumination for 20 min. The photocathode was illuminated at 100 mWcm^{-2} before measuring the OCP decay. (c) Carrier lifetime dependence on OCP of the photocathode. (d) Electrochemical impedance spectroscopy (EIS) measurement of $p\text{-Si/SiO}_x/\text{MoS}_2$ of 500-ALD-cycle photocathode under dark (black) and under illuminated condition (red, inserted).

Figure 6b denotes the OCP voltage decay after 20 min of illumination and Figure 6c shows the hole lifetime determined from the results. The long lifetime of 60 s for the photocathode confirms that the $p\text{-Si/SiO}_x/\text{MoS}_2$ structure effectively prevented surface recombination with the electrolyte. The fast charge transfer kinetics could be further understood by combining the EIS measurements of our $p\text{-Si/SiO}_x/\text{MoS}_2$ photocathode shown in Figure 6d. The charge transfer characteristics can be analyzed by means of an equivalent circuit model (Figure S2b), and the circuit parameters are derived from fitting Nyquist plots. In Figure 6d, EIS measurements on 500-ALD-cycle photocathodes under dark and illumination are presented. The overall charge transfer resistance was dramatically reduced under the illumination condition (red inserted) compared to the dark equilibrium condition. Under illumination, for 500-ALD-cycle photocathode, the charge transfer resistance (R_{MoS_2}) of $22.38 \Omega \cdot \text{cm}^2$ at the $\text{MoS}_2/\text{electrolyte}$ interface, and the $p\text{-Si}/\text{MoS}_2$ junction resistance (R_{jc}) of $27.38 \Omega \cdot \text{cm}^2$ were obtained, confirming the facile kinetics of the photocathode and are catalytically active. The Nyquist plot shows the two distinctive semicircles, which represent the frequency-dependent resistance-capacitance (RC) characteristics. The equivalent circuit, which is depicted in Supporting Figure S2b consists of constant phase elements coupled with the charge transfer resistance. Measured parameters are summarized in Table S1. R_{jc} refers to the charge transfer resistance at the $p\text{-Si}/\text{MoS}_2$ junction, R_{MoS_2} is the charge transfer resistance between the MoS_2 and the electrolyte, respectively. Note that under illumination, the R_{jc} and R_{MoS_2} significantly decreased more than an order of magnitude compared with that of the dark equilibrium condition, which depicted the induced

voltage drop across the. R_{MoS_2} , charge transfer resistance can be derived from the impedance scan of the low-frequency range, the charge transfer resistance at junction R_{jc} , and bulk resistance R_{bulk} from the mid-frequency range to high frequency. Q_{jc} is the junction space charge region capacitance and Q_{MoS_2} is the MoS_2 /electrolyte interface capacitance. The MoS_2 /electrolyte resistance was the lowest for the 300 ALD cycle photocathode, which is due to the vertical layers and exposure of the edge sites. The resistance values for 500 ALD cycles photocathode are somewhat higher than those of the 300 ALD cycle photocathode. The second semicircle, which corresponds to the capacitance-resistance (RC) through the p - i - n junction, indicates that the illumination increases the junction voltage.

Finally, we systematically propose the degree of band bending qualitatively when employing mixed-phase metal chalcogenides on Si for application in PEC water splitting. First of all, the issues of FLP_{ss} could be cleared by ALD passivation. The other would be Fermi-level pinning (FLP_{ns}) by nanoscale Schottky junctions (p -Si/1T MoS_2) [57]. When it comes to the metallic 1T MoS_2 contacted with Si, which forms the increased Schottky barrier height by environmental Fermi-level pinning. Moreover, it has trade-off effects by Fermi-level depinning (FLDP_{ox}) by the presence of oxide interfaces, i.e., SiO_x [58]. We suspect that these mechanisms cancel out each other in V_{ph} enhancements. Because of the discontinuous nature of the deposited layers (based on metallic 1T MoS_2), electrical charges are screened only partially, inducing discontinuous junctions. This is also responsible for V_{ph} increase although the junction properties are not the same as the bulk counterpart. Such a conclusion is plausible as studies on the thickness dependence of catalyst layers on the junction characteristics, insisting that the catalyst layer thinner than the Debye length only partially screen charges with nonideal characteristics. Note that in such PEC systems, the currents flow not only through the nanoscale Schottky (metal-semiconductor) junctions but also through semiconductor-electrolyte interfaces. This differs from conventional solid-state devices and was systematically studied by Rossi and Lewis [59]. Therefore, pinch-off effects by Fermi-level depinning ($\text{FLDP}_{\text{inhm}}$) operates from inhomogeneous Schottky junctions at the nanoscale.

3. Experimental Section

3.1. Atomic Layer Deposition

Atomic layer deposition of the MoS_2 films. The MoS_2 film was grown on a p -type silicon wafer (Boron doped, 1–30 Ωcm , $525 \pm 25 \mu\text{m}$ thickness) using a custom-designed ALD system. The silicon wafer was cleaned with piranha solution, a 3:1 mixture of concentrated sulfuric acid (H_2SO_4) with hydrogen peroxide (H_2O_2), for 20 min to remove any organic residues on the surface, followed by immersion in buffered oxide etch or BOE ($\text{HF}:\text{NH}_4\text{F}$ 7:1) to remove the native oxides. The chamber was heated and stabilized for 30 min before reactants were introduced. The MoS_2 thin film was deposited at a temperature range of 250–300 $^\circ\text{C}$ using MoCl_5 (99.6%, Strem Chemicals, Inc., Newburyport, MA, USA) and H_2S (3.99%, balanced N_2 , JC Gas, Daegu, Korea) and a carrier gas of Ar (5N, JC Gas, Daegu, Korea). The pulse time was controlled to be 0.2 s followed by 15 s of purging with Ar at a gas flow of 50 sccm.

3.2. Material Characterization

The morphology of the MoS_2 film was observed by field-emission scanning electron microscopy (FESEM; JS7500F, JEOL, Tokyo, Japan). Cross-sectional images were obtained by focus ion-beam etching (SMI305TB, SII, Chiba, Japan), and high-resolution transmission electron microscopy (HRTEM; JEM2100F, JEOL, Tokyo, Japan). Chemical compositions of the surface were analyzed by X-ray photoelectron spectroscopy (XPS; ESCA sigma Probe, Thermo VG Scientific, Waltham, MA, USA). MoS_2 formation was characterized by Raman spectroscopy (RM1000 microprobe, Renishaw, Wharton Anderch, UK). Structure analysis using energy-dispersive X-ray spectroscopy (Aztec, Oxford Instruments, Oxford, UK) was conducted.

3.3. Electrochemical Characterization

All electrochemical measurements were performed using a three-electrode system with Ag/AgCl as the reference electrode, a Pt wire (diameter of 0.5 mm) as the counter electrode and MoS₂ on a silicon substrate as the working electrode. Cyclic voltammetry and linear sweep voltamperometry were performed using a VMP3 Potentiostat from Bio-Logic at a scan rate of 50 mV/s in 0.5 M of H₂SO₄ (pH 0.3) as the electrolyte. For illuminated OCP measurements, 5–10 samples from different batches for each cycle were taken and a solar simulator (Oriel Sol 301A, Newport) with a Keithely 2400 source meter was used under AM 1.5 illumination (100 mW cm^{−2}). Electrochemical impedance spectra were measured over a frequency range of 10⁶ to 0.1 Hz at 0 vs. the reversible hydrogen electrode (RHE). The Mott-Schottky impedance was performed at 300 kHz to 1 kHz at a bias of −0.6 V to 0 V vs. RHE at 1 sun illumination. The electrode area was 0.785 cm². To make an ohmic contact, the back side of the silicon was scratched with a diamond cutter, followed by a Gallium–Indium eutectic alloy and stuck to the copper electrode using silver paste epoxy. Magnetic stirring at 500 rpm was performed during the experiment.

4. Conclusions

Our chlorine-rich, ALD-grown MoS₂ was deposited with different cycles on lightly doped *p*-Si. Neither a high-temperature sulfurization process nor any interface engineering was necessary due to the mixed-phase characteristics of the MoS₂ thin film. Thickness-dependent PEC characteristics were theoretically demonstrated along with experimental results. Our photocathodes showed the anodic shift of 0.47 V compared to bare *p*-Si with a saturation J_{ph} of 30 mA·cm^{−2} and excellent stability (75 h under 1 sun illumination). ALD-grown MoS₂ film can induce energy band bending, resulting in a V_{ph} enhancement, which coincides with a bulk *p-i-n* junction model. The energetically favorable charge transfer mechanism is introduced for the embedded metallic 1T phase MoS₂.

Supplementary Materials: The following are available online at <http://www.mdpi.com/2073-4344/8/12/580/s1>, Figure S1: Schematic energy level diagram of the band alignment at *p*-Si/MoS₂ interface in terms of vacuum level and normal hydrogen electrode level in electrolyte of pH = 0.3. The *p*-Si doping level is $\sim 1.6 \times 10^{15}$ cm^{−3}, Figure S2: (a) Nyquist plot of 700-ALD-cycles and 300-ALD-cycles on *p*-Si photocathode under 1sun illumination at 0 bias. (b) Equivalent circuit corresponding to the EIS measurement. R_{bulk} is bulk resistance of the silicon, Q_{jc} is constant phase element (CPE) of *p*-Si/MoS₂ junction along with junction resistance R_{jc} , CPE of MoS₂/electrolyte interface is denoted as Q_{MoS_2} and the resistance of R_{MoS_2} , Table S1: Measured charge transfer resistances.

Author Contributions: Conceptualization, C.B., J.J. and H.S.; Methodology, J.J., C.B., E.K. and T.A.H.; Writing-Original Draft Preparation, J.J.; Writing-Review & Editing, C.B. and H.S.; Supervision, C.B., H.Y., J.H.P., and H.S.

Funding: The authors acknowledge the grant by the National Research Foundation of Korea (NRF-2018R1D1A1B07051059, NRF-2016M3D1A1027664, NRF-2018M3C1B7020716 and NRF-2018K1A3A1A32055268).

Conflicts of Interest: The authors declare no conflict of interest.

References

1. Sivula, K.; van de Krol, R. Semiconducting materials for photoelectrochemical energy conversion. *Nat. Rev. Mater.* **2016**, *1*, 15010. [CrossRef]
2. Xing, Z.; Ren, F.; Wu, H.; Wu, L.; Wang, X.; Wang, J.; Wan, D.; Zhang, G.; Jiang, C. Enhanced PEC performance of nanoporous Si photocathodes by converting HfO₂ and TiO₂ passivation layers. *Sci. Rep.* **2017**, *7*, 43901. [CrossRef] [PubMed]
3. Kim, J.H.; Jang, J.W.; Jo, Y.H.; Abdi, F.F.; Lee, Y.H.; van de Krol, R.; Lee, J.S. Hetero-type dual photoanodes for unbiased solar water splitting with extended light harvesting. *Nat. Commun.* **2017**, *7*, 13380. [CrossRef] [PubMed]
4. Choi, M.J.; Jung, J.Y.; Park, M.J.; Song, J.W.; Lee, J.H.; Bang, J.H. Long-term durable silicon photocathode protected by a thin Al₂O₃/SiO_x layer for photoelectrochemical hydrogen evolution. *J. Mater. Chem. A* **2014**, *2*, 2928–2933. [CrossRef]

5. Zhao, Y.; Anderson, N.C.; Zhu, K.; Aguiar, J.A.; Seabold, J.A.; Lagemaat, J.V.D.; Oh, J. Oxidatively Stable Nanoporous Silicon Photocathodes with Enhanced Onset Voltage for Photoelectrochemical Proton Reduction. *Nano Lett.* **2015**, *15*, 2517–2525. [[CrossRef](#)] [[PubMed](#)]
6. Feng, J.; Gong, M.; Kenney, M.J.; Wu, J.Z.; Zhang, B.; Li, Y.; Dai, H. Nickel-coated silicon photocathode for water splitting in alkaline electrolytes. *Nano Res.* **2015**, *8*, 1577–1583. [[CrossRef](#)]
7. Wickramaratne, D.; Zahid, F.; Lake, R.K. Electronic and thermoelectric properties of few-layer transition metal dichalcogenides. *J. Chem. Phys.* **2014**, *140*, 124710. [[CrossRef](#)] [[PubMed](#)]
8. Wang, S.; Tian, H.; Ren, C.; Yu, J.; Sun, M. Electronic and optical properties of heterostructures based on transition metal dichalcogenides and graphene-like zinc oxide. *Sci. Rep.* **2018**, *8*, 12009. [[CrossRef](#)] [[PubMed](#)]
9. Lang, O.; Tömm, V.; Schlaf, R.; Pettenkofer, C.; Jaegermann, W. Single crystalline GaSe/WeSe₂ heterointerfaces grown by van der Waals epitaxy. II. Junction characterization. *J. Appl. Phys.* **1994**, *75*, 7814–7820. [[CrossRef](#)]
10. Andoshe, D.M.; Jin, G.; Lee, C.S.; Kim, C.; Kwon, K.C.; Choi, S.; Sohn, W.; Moon, C.W.; Lee, S.H.; Suh, J.M.; et al. Directly Assembled 3D Molybdenum Disulfide on Silicon Wafer for Efficient Photoelectrochemical Water Reduction. *Adv. Sustain. Syst.* **2018**, *2*, 1700142–1700151. [[CrossRef](#)]
11. Xiang, Q.; Yu, J.; Jaroniec, M. Synergetic effect of MoS₂ and graphene as cocatalysts for enhanced photocatalytic H₂ production activity of TiO₂ nanoparticles. *J. Am. Chem. Soc.* **2012**, *134*, 6575–6578. [[CrossRef](#)] [[PubMed](#)]
12. Chang, K.; Mei, Z.; Wang, T.; Kang, Q.; Ouyang, S.; Ye, J. MoS₂/graphene cocatalyst for efficient photocatalytic H₂ evolution under visible light irradiation. *ACS Nano* **2014**, *8*, 7078–7087. [[CrossRef](#)] [[PubMed](#)]
13. Li, Y.; Wang, H.; Peng, S. Tunable Photodeposition of MoS₂ onto a Composite of Reduced Graphene Oxide and CdS for Synergic Photocatalytic Hydrogen Generation. *J. Phys. Chem. C* **2014**, *118*, 19842–19848. [[CrossRef](#)]
14. Karunadasa, H.I.; Montalvo, E.; Sun, Y.; Majda, M.; Long, J.R.; Chang, C.J. A molecular MoS₂ edge site mimic for catalytic hydrogen generation. *Science* **2012**, *335*, 698–702. [[CrossRef](#)] [[PubMed](#)]
15. Li, Z.; Meng, X.; Zhang, Z. Recent Development on MoS₂-based Photocatalysis: A Review. *J. Photochem. Photobiol. C Photochem. Rev.* **2017**, *25*, 39–55. [[CrossRef](#)]
16. Hinnemann, B.; Moses, P.G.; Bonde, J.; Jørgensen, K.P.; Nielsen, J.H.; Hørch, S.; Chorkendorff, I.; Nørskov, J.K. Biomimetic hydrogen evolution: MoS₂ nanoparticles as catalyst for hydrogen evolution. *J. Am. Chem. Soc.* **2005**, *127*, 5308–5309. [[CrossRef](#)] [[PubMed](#)]
17. Oh, S.; Kim, J.B.; Song, J.T.; Oh, J.; Kim, S.-H. Atomic layer deposited Molybdenum disulfide on Si photocathodes for highly efficient photoelectrochemical water reduction reaction. *J. Mater. Chem. A* **2017**, *5*, 3304–3310. [[CrossRef](#)]
18. Yin, Y.; Zhang, Y.; Gao, T.; Yao, T.; Zhang, X.; Han, J.; Wang, X.; Zhang, Z.; Xu, P.; Zhang, P.; et al. Synergistic Phase and Disorder Engineering in 1T-MoSe₂ Nanosheets for Enhanced Hydrogen Evolution Reaction. *Adv. Mater.* **2017**, *29*, 1700311. [[CrossRef](#)] [[PubMed](#)]
19. Lukowski, M.A.; Daniel, A.S.; Meng, F.; Forticaux, A.; Li, L.; Jin, S. Enhanced Hydrogen Evolution Catalysis from Chemically Exfoliated Metallic MoS₂ Nanosheets. *J. Am. Chem. Soc.* **2013**, *135*, 10274–10277. [[CrossRef](#)] [[PubMed](#)]
20. Voiry, D.; Salehi, M.; Silva, R.; Fujita, T.; Chen, M.; Asefa, T.; Shenoy, V.B.; Eda, G.; Chhowalla, M. Conducting MoS₂ Nanosheets as Catalysts for Hydrogen Evolution Reaction. *Nano Lett.* **2013**, *13*, 6222–6227. [[CrossRef](#)] [[PubMed](#)]
21. Hill, J.C.; Landers, A.T.; Switzer, J.A. An electrodeposited inhomogeneous metal–insulator–semiconductor junction for efficient photoelectrochemical water oxidation. *Nat. Mater.* **2015**, *14*, 1150–1155. [[CrossRef](#)] [[PubMed](#)]
22. Thorne, J.E.; Li, S.; Du, C.; Qin, G.; Wang, D. Energetics at the Surface of Photoelectrodes and Its Influence on the Photoelectrochemical Properties. *J. Phys. Chem. Lett.* **2015**, *6*, 4083–4088. [[CrossRef](#)] [[PubMed](#)]
23. Kwon, K.C.; Choi, S.; Hong, K.; Moon, C.W.; Shim, Y.-S.; Kim, D.H.; Kim, T.; Sohn, W.; Jeon, J.-M.; Lee, C.-H.; et al. Wafer-scale transferable molybdenum disulfide thin-film catalysts for photoelectrochemical hydrogen production. *Energy Environ. Sci.* **2016**, *9*, 2240–2248. [[CrossRef](#)]

24. Seo, J.; Kim, H.J.; Pekarek, R.T.; Rose, M.J. Hybrid Organic/Inorganic Band-Edge Modulation of p-Si(111) Photoelectrodes: Effects of R, Metal Oxide, and Pt on H₂ Generation. *J. Am. Chem. Soc.* **2015**, *137*, 3173–3176. [[CrossRef](#)] [[PubMed](#)]
25. Benck, J.D.; Lee, S.C.; Fong, K.D.; Kibsgaard, J.; Sinclair, R.; Jaramillo, T.F. Designing Active and Stable Silicon Photocathodes for Solar Hydrogen Production Using Molybdenum Sulfide Nanomaterials. *Adv. Energy Mater.* **2014**, *4*, 1400739–1400747. [[CrossRef](#)]
26. Digdaya, I.A.; Adhyaksa, G.W.; Trześniewski, B.J.; Garnett, E.C.; Smith, W.A. Interfacial engineering of metal-insulator-semiconductor junctions for efficient and stable photoelectrochemical water oxidation. *Nat. Commun.* **2017**, *8*, 15968. [[CrossRef](#)] [[PubMed](#)]
27. Fan, R.; Mao, J.; Yin, Z.; Jie, J.; Dong, W.; Fang, L.; Zheng, F.; Shen, M. Efficient and Stable Silicon Photocathodes Coated with Vertically Staining Nano-MoS₂ Films for Solar hydrogen Production. *ACS Appl. Mater. Interfaces* **2017**, *9*, 6123–6129. [[CrossRef](#)] [[PubMed](#)]
28. Lin, Y.; Battaglia, C.; Boccard, M.; Hettick, M.; Yu, Z.; Ballif, C.; Ager, J.W.; Javey, A. Amorphous Si thin film based photocathodes with high photovoltage for efficient hydrogen production. *Nano Lett.* **2013**, *13*, 5615–5618. [[CrossRef](#)] [[PubMed](#)]
29. Ho, T.A.; Bae, C.; Lee, S.; Kim, M.; Montero-Moreno, J.M.; Park, J.H.; Shin, H. Edge-On MoS₂ Thin Films by Atomic Layer Deposition for Understanding the Interplay between the Active Area and Hydrogen Evolution Reaction. *Chem. Mater.* **2017**, *29*, 7604–7614. [[CrossRef](#)]
30. Joensen, P.; Crozier, E.; Alberding, N.; Frindt, R. A study of single-layer and restacked MoS₂ by X-ray diffraction and X-ray absorption spectroscopy. *J. Phys. C Solid State Phys.* **1987**, *20*, 4043–4053. [[CrossRef](#)]
31. Sim, U.; Yang, T.-Y.; Moon, J.; An, J.; Hwang, J.; Seo, J.-H.; Lee, J.; Kim, K.Y.; Lee, J.; Han, S.; et al. N-doped monolayer graphene catalyst on silicon photocathode for hydrogen production. *Energy Environ. Sci.* **2013**, *6*, 3658–3664. [[CrossRef](#)]
32. Walter, M.G.; Warren, E.L.; McKone, J.R.; Boettcher, S.W.; Mi, Q.; Santori, E.A.; Lewis, N.S. Solar Water Splitting cells. *Chem. Rev.* **2010**, *110*, 6446–6473. [[CrossRef](#)] [[PubMed](#)]
33. Esposito, D.V.; Levin, I.; Moffat, T.P.; Talin, A.A. H₂ evolution at Si-based metal-insulator-semiconductor photoelectrodes enhanced by inversion channel charge collection and H spillover. *Nat. Mater.* **2013**, *12*, 562–568. [[CrossRef](#)] [[PubMed](#)]
34. Weitering, H.H.; Ettema, A.R.H.F.; Hibma, T. Surface states and Fermi-level pinning at epitaxial Pb/Si(111) surfaces. *Phys. Rev. B* **1992**, *45*, 9126–9135. [[CrossRef](#)]
35. Liu, D.; Li, L.; Gao, Y.; Wang, C.; Jiang, J.; Xiong, Y. The Nature of Photocatalytic “Water Splitting” on Silicon Nanowires. *Angew. Chem. Int. Ed.* **2015**, *54*, 2980–2985. [[CrossRef](#)] [[PubMed](#)]
36. Kronik, L.; Shapira, Y. Surface photovoltage phenomena: Theory, experiment, and applications. *Surf. Sci. Rep.* **1999**, *37*, 1–206. [[CrossRef](#)]
37. Benson, J.; Li, M.; Wang, S.; Wang, P.; Papakonstantinou, P. Electrocatalytic Hydrogen Evolution Reaction on Edges of a Few Layer Molybdenum Disulfide Nanodots. *ACS Appl. Mater. Interfaces* **2015**, *7*, 14113–14122. [[CrossRef](#)] [[PubMed](#)]
38. Thorne, J.E.; Jang, J.W.; Liu, E.Y.; Wang, D. Understanding the origin of photoelectrode performance enhancement by probing surface kinetics. *Chem. Sci.* **2016**, *7*, 3347–3354. [[CrossRef](#)] [[PubMed](#)]
39. Quickenden, T.I.; Yim, G.K. The relationship between open circuit photovoltage and light intensity in photogalvanic cells—An extension of albery and Archer’s treatment. *Electrochem. Acta* **1979**, *24*, 143–146. [[CrossRef](#)]
40. Salvador, P.; Hidalgo, M.G.; Zaban, A.; Bisquert, J. Illumination intensity dependence of the photovoltage in nanostructured TiO₂ dye-sensitized solar cells. *J. Phys. Chem. B* **2005**, *109*, 15915–15926. [[CrossRef](#)] [[PubMed](#)]
41. Liu, W.; Zhang, Y. Electrical characterization of TiO₂/CH₃NH₃PbI₃ heterojunction solar cells. *J. Mater. Chem. A* **2014**, *2*, 10244–10249. [[CrossRef](#)]
42. Kirchartz, T.; Gong, W.; Hawks, S.A.; Agostinelli, T.; MacKenzie, R.C.I.; Yang, Y.; Nelson, J. Sensitivity of the Mott–Schottky Analysis in Organic Solar Cells. *J. Phys. Chem. C* **2012**, *116*, 7672–7680. [[CrossRef](#)]
43. Kenney, M.J.; Gong, M.; Li, Y.; Wu, J.Z.; Feng, J.; Lanza, M.; Dai, H. High-performance silicon photoanodes passivated with ultrathin nickel films for water oxidation. *Science* **2013**, *342*, 836–840. [[CrossRef](#)] [[PubMed](#)]
44. Fujii, K.; Ono, M.; Iwaki, Y.; Sato, K.; Ohkawa, K.; Yao, T. Photoelectrochemical Properties of the p–n Junction in and near the Surface Depletion Region of n-Type GaN. *J. Phys. Chem. C* **2010**, *114*, 22727–22735. [[CrossRef](#)]

45. Ding, Q.; Meng, F.; English, C.R.; Cabán-Acevedo, M.; Shearer, M.J.; Liang, D.; Daniel, A.S.; Hamers, R.J.; Jin, S. Efficient photoelectrochemical hydrogen generation using heterostructures of Si and chemically exfoliated metallic MoS₂. *J. Am. Chem. Soc.* **2014**, *136*, 8504–8507. [[CrossRef](#)] [[PubMed](#)]
46. Du, P.; Zhu, Y.; Zhang, J.; Xu, D.A.; Peng, W.; Zhang, G.; Zhang, F.; Fan, X. Metallic 1T phase MoS₂ nanosheets as a highly efficient co-catalyst for the photocatalytic hydrogen evolution of CdS nanorods. *RSC Adv.* **2016**, *6*, 74394–74399. [[CrossRef](#)]
47. Bai, H.F.; Xu, L.C.; Di, M.Y.; Hao, L.Y.; Yang, Z.; Liu, R.P.; Li, X.Y. The intrinsic interface properties of the top and edge 1T/2H MoS₂ contact: A first-principles study. *J. Appl. Phys.* **2018**, *123*, 95301–95306. [[CrossRef](#)]
48. Reichman, J. The current-voltage characteristics of semiconductor-electrolyte junction photovoltaic cells. *Appl. Phys. Lett.* **1980**, *36*, 574–577. [[CrossRef](#)]
49. Bard, A.; Faulkner, L. *Electrochemical Methods. Fundamentals and Applications*, 2nd ed.; John Wiley and Sons: New York, NY, USA, 2001.
50. Claeys, C.L.; Watanabe, M.; Rai-Choudhury, P.; Stallhofer, P. *High Purity Silicon*; The Electrochemical Society, Inc.: Burghausen, Germany, 2002.
51. Benchamekh, R.; Nesoklon, M.; Jancu, J.-M.; Voisin, P. *Semiconductor Modeling Techniques*; Springer: Berlin/Heidelberg, Germany, 2012.
52. Schmidt, H.; Giustiniano, F.; Eda, G. Electronic transport properties of transition metal dichalcogenide field-effect devices: Surface and interface effects. *Chem. Soc. Rev.* **2015**, *44*, 7715–7736. [[CrossRef](#)] [[PubMed](#)]
53. Wang, H.; Zhang, C.; Rana, F. Ultrafast Dynamics of Defect-Assisted Electron–Hole Recombination in Monolayer MoS₂. *Nano Lett.* **2015**, *15*, 339–345. [[CrossRef](#)] [[PubMed](#)]
54. Yun, W.S.; Han, S.; Hong, S.C.; Kim, I.G.; Lee, J. Thickness and strain effects on electronic structures of transition metal dichalcogenides: 2H-MX₂ (M = Mo, W; X = S, Se, Te) semiconductors. *Phys. Rev. B* **2012**, *85*, 33305–33310. [[CrossRef](#)]
55. Hayden, T.; Dumesic, J.; Sherwood, R.; Baker, R. Direct Observation by Controlled Atmosphere Electron Microscopy of the Changes in Morphology of Molybdenum Oxide and Sulfide Supported on Alumina and Graphite. *J. Catal.* **1987**, *105*, 299–318. [[CrossRef](#)]
56. Li, T.-L.; Lee, Y.-L.; Teng, H. High-performance quantum dot-sensitized solar cells based on sensitization with CuInS₂ quantum dots/CdS heterostructure. *Energy Environ. Sci.* **2012**, *5*, 5315–5324. [[CrossRef](#)]
57. Agrawal, A.; Lin, J.; Barth, M.; White, R.; Zheng, B.; Chopra, S.; Gupta, S.; Wang, K.; Gelatos, J.; Mohnney, S.E.; et al. Fermi level depinning and contact resistivity reduction using a reduced titania interlayer in n-silicon metal-insulator-semiconductor ohmic contacts nanowire array electrode to construct a photocathode composed of elements abundant on the earth for hydrogen generation. *Appl. Phys. Lett.* **2014**, *104*, 112101.
58. Smit, G.D.J.; Rogge, S.; Klapwijk, T.M. Scaling of nano-Schottky-diodes. *Appl. Phys. Lett.* **2002**, *81*, 3852–3854. [[CrossRef](#)]
59. Rossi, R.C.; Lewis, N.S. Investigation of the Size-Scaling Behavior of Spatially Nonuniform Barrier Height Contacts to Semiconductor Surfaces Using Ordered Nanometer-Scale Nickel Arrays on Silicon Electrodes. *J. Phys. Chem. B* **2001**, *105*, 12303–12318. [[CrossRef](#)]

